



# Enhancing Hyperspectral Image Resolution with Deep Transfer Learning: A Case Study on Model Deployment and Evaluation

Nafis Khan, Siddharth Misra, James Omeke\*, Priyanka Chukka, Siddhanth Sirg Kapoor

Department of Petroleum Engineering, Texas A&M University, College Station, Texas, United States of America

## ABSTRACT

Hyperspectral imaging holds immense potential for detailed land cover analysis due to its rich spectral information across the electromagnetic spectrum. However, the inherent trade-off between spatial and spectral resolution limits its applicability. The study explores the deployment and enhancement of Single Hyperspectral Image Super-Resolution (SSPSR) model, using the Spatial-Spectral Prior Network (SSPN), to notably improve the spatial and spectral quality of hyperspectral images. This model stands out for its ability to elevate image resolution without relying on supplementary hardware enhancements. Our research focused on training this model using the comprehensive Chikusei dataset, this dataset features 128 spectral bands from 363 nm to 1018 nm, captured over Chikusei, Japan, enhancing deep learning research in agricultural and urban land cover analysis, followed by fine-tuning with the Cave dataset, renowned for its hyperspectral indoor images across numerous spectral bands, to ensure adaptability to diverse real-world scenarios. A refined loss function was introduced to enhance image fidelity, spatial smoothness, spectral fidelity and perceptual quality. Through meticulous hyper parameter tuning and leveraging of public datasets, we significantly improved upon existing methodologies, as evidenced by quantitative performance measures. The fine-tuned SSPSR model achieved noteworthy gains in Peak Signal-to-Noise Ratio (PSNR) and Structural Similarity Index (SSIM); thus, contributing to the precision and efficiency of hyperspectral image analysis. Our results demonstrate the model's enhanced performance in generating high-resolution images from low-resolution data, promising substantial advancements in remote sensing and land mapping applications.

**Keywords:** Image resolution; Spatial resolution; Remote sensing; Deep transfer learning; Hyperspectral images; Machine learning

## INTRODUCTION

Unlike traditional RGB images, hyperspectral images capture a vast amount of spectral data for each pixel, encompassing the entire electromagnetic spectrum. This creates a three-dimensional "data cube" where the additional dimension represents spectral information. Each pixel's unique spectrum acts like a fingerprint, allowing scientists to identify materials present. This rich data empowers researchers in numerous fields. In agriculture, hyperspectral imaging helps assess crop health and optimize practices. For mineral exploration, it aids in identifying and mapping valuable resources. Even cultural heritage preservation benefits, as art analysis can reveal hidden layers and assess an artwork's condition. By capturing light's complex story at each image point, hyperspectral imaging unlocks a deeper understanding of our world.

Hyperspectral imaging, with its ability to capture data from

numerous frequency bands across the electromagnetic spectrum, has been widely used in various applications. Lu et al., provides a comprehensive review of its use in medical diagnostics and image-guided surgery, highlighting its ability to capture spatially resolved spectral images [1]. Kurz et al., Bahalul et al., both explore its potential in close-range applications, with Kurz emphasizing its flexibility and high spectral resolution and Bahalul introducing a new approach using wave front division interference [2,3]. These studies collectively underscore the versatility and potential of hyperspectral imaging in various fields. Peyghambari et al., Kwan both highlight the potential of hyperspectral imaging in geological mapping and remote sensing applications, respectively [4,5]. However, the trade-off between spatial and spectral resolution in remote sensing is a key consideration, which can be mitigated by deep learning-based super-resolution techniques [4]. The enhancement of spectral resolution in hyperspectral images is also a focus, with Fotiadou et al., proposing a machine learning

**Correspondence to:** James Omeke, Department of Petroleum Engineering, Texas A&M University, College Station, Texas, United States of America, Email: jamesomeke@gmail.com

**Received:** 19-Oct-2024, Manuscript No. JGRS-24-27215; **Editor assigned:** 21-Oct-2024, PreQC No. JGRS-24-27215 (PQ); **Reviewed:** 07-Nov-2024, QC No. JGRS-24-27215; **Revised:** 15-Nov-2024, Manuscript No. JGRS-24-27215 (R); **Published:** 22-Nov-2024, DOI: 10.35248/2469-4134.24.13.358

**Citation:** Khan N, Misra S, Omeke J, Chukka P, Sirg Kapoor S (2024). Enhancing Hyperspectral Image Resolution with Deep Transfer Learning: A Case Study on Model Deployment and Evaluation. J Remote Sens GIS. 13:358.

**Copyright:** © 2024 Khan N, et al. This is an open-access article distributed under the terms of the Creative Commons Attribution License, which permits unrestricted use, distribution, and reproduction in any medium, provided the original author and source are credited.

technique using sparse representations [6]. Ablin et al., further discusses the challenges and prospects of hyperspectral image classification, emphasizing the need to reduce uncertainties in the image processing chain [7].

In Figure 1, the left side illustrates how increased spatial resolution leads to a finer grained representation of the image data, whereas the right side depicts spectral resolution, indicating the sensor's ability to discriminate between narrow wavelength intervals, important for identifying and classifying diverse materials based on their spectral signatures. To measure high spectral resolution *versus* high spatial resolution, different types of equipment or sensor technologies are required due to the differing nature of the data they capture.

The field of hyperspectral imaging presents a unique challenge for traditional analysis methods due to the high dimensionality and complex spectral information contained within each pixel. Machine Learning (ML) algorithms are emerging as powerful tools to address these complexities and unlock the full potential of hyperspectral data. ML techniques excel in automating workflows such as classification, anomaly detection and target recognition, significantly reducing the burden of manual analysis for hyperspectral datasets. Furthermore, ML facilitates feature extraction, identifying the most relevant spectral signatures within the data for a specific application. This targeted approach leads to improved accuracy in material classification and anomaly detection compared to conventional methods. Moreover, the ability of ML models to learn from labelled datasets fosters continuous improvement in performance. By generalizing knowledge acquired from diverse hyperspectral datasets, these models can be effectively applied across a wider range of applications and environments. Finally, ML offers dimensionality reduction techniques that compress the high-dimensional hyperspectral data while preserving critical information. This not only enhances computational efficiency but also facilitates faster and more streamlined analysis. In conclusion, machine learning serves as a foundation for unlocking the true power of hyperspectral data, empowering researchers with automated workflows, improved feature extraction, enhanced

accuracy and efficient data analysis capabilities. Caponi et al., Wu et al., used machine learning on images to extract physical properties of interest [8,9]. Misra et al., Li et al., used deep learning techniques of T1-T2 heat maps for purposes of signal synthesis as a reconstruction approach [10,11]. Wu et al., developed a workflow for connectivity quantification by processing images using traditional machine learning guided by strong feature extraction techniques [12].

Recent research has made significant progress in hyperspectral image super-resolution using deep learning and transfer learning. Yuan et al., Liu et al., both proposed frameworks that leverage the relationship between low- and high-resolution images, with Yuan specifically focusing on the spectral characteristic [13,14]. Li et al., introduced a deep unsupervised fusion-learning framework that generates a latent high-resolution hyperspectral image using only the observed low-resolution hyperspectral and high-resolution RGB images [15]. Huang utilized a Generative Adversarial Network (GAN) and residual learning for hyperspectral image super-resolution, achieving superior performance in spectral fidelity and spatial resolution [16]. Zou combined Deep Residual Convolutional Neural Network (DRCNN) with spectral unmixing, preserving spatial and spectral information without the need for auxiliary images [17].

Wang et al., developed a deep residual convolutional neural network with 18 convolution layers, achieving improved hyperspectral super-resolution results [18]. In exploring advancements in hyperspectral image super-resolution, our study is particularly inspired by the innovative techniques developed by Jiang and Liu [14,19]. Jiang's introduction of the SSPSR model, which features a SSPN, presents an innovative approach to enhancing hyperspectral imagery [19]. This model adeptly navigates the challenges posed by the high-dimensional spectral data and the scarcity of training samples. It uses group convolution with shared parameters and a progressive up sampling strategy, markedly improving the spatial and spectral quality of images [20]. Similarly, Liu advances this field with the proposal of a Spatial-Spectral Feedback Network (SSFN), further enriching the methodology for hyperspectral image analysis.

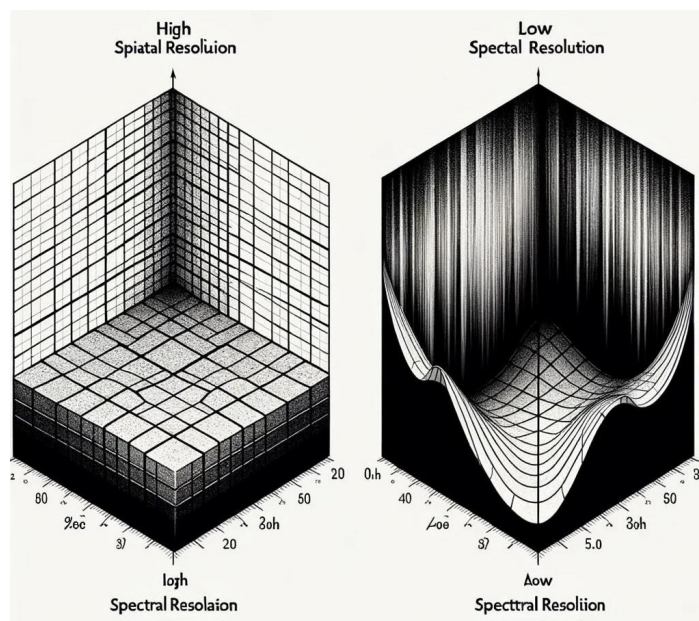


**Figure 1:** Visual distinction between the concepts of spatial and spectral resolutions, which are the essential components of hyperspectral image analysis.

The SSPSR model, with its capacity to significantly elevate image detail and resolution while ensuring stable training, outperforms existing methods and establishes a new standard. The alignment of these methodologies with our research objectives has led us to adopt Jiang et al., SSPSR model for our study, aiming to leverage its strengths in enhancing hyperspectral imagery's spatial and spectral fidelity [19]. Our approach involves training the SSPSR model on the Chikusei dataset [21]. Fine-tuning its hyper-parameters and refining its performance on the Cave dataset [22]. This process resulted in heightened adaptability and improved overall performance, showcasing the efficacy of hyper-parameter-tuning and fine-tuning methodologies in hyperspectral image super-resolution tasks.

## MATERIALS AND METHODS

### Objectives

This study aims to deploy and evaluate the precision and efficiency of hyperspectral image analysis using a deep learning technique, SSPSR, developed by Jiang et al. [19]. Our goal will be the following:

- Achieve high spatial and spectral accuracy in hyperspectral images.
- Reduce computational time required for super-resolution processing

To attain these objectives, the following methodologies were applied:

**Super-resolution enhancement:** Utilized deep learning techniques, particularly SSPSR, to upscale low-resolution hyperspectral images.

**Model development:** Improved a deep learning model to simultaneously enhance spatial and spectral accuracies, ensuring precise object placement and accurate spectral data representation.

**Process optimization:** Streamlined super-resolution enhancement by implementing computational strategies that expedited data processing.

**Technique adaptation:** Modified the SSPSR architecture to better fit the complexities of hyperspectral image enhancement, focusing on training protocols that improve spatial detail and spectral fidelity.

**Performance benchmarking:** Conducted quantitative assessments of model performance using indices like PSNR and SSIM to ensure spatial and spectral precision.

**Model fine-tuning:** Adjusted hyper parameters to balance image resolution precision with model complexity, optimizing for the most effective learning process

**Computational resources:** The training was conducted on a system with 32 GB RAM, an NVIDIA RTX 2080 GPU and an Intel i7 processor. The training time for the SSPSR model was approximately 10 h for 40 epochs. The inferencing time on new datasets was around 30 sec per image.

### Resources and validation

The project utilized and validated its methodologies through:

**Model training and testing:** Chikusei dataset is used for a comprehensive training, validation, testing and benchmarking. The training dataset comprised 3700 samples, while the testing dataset included 370 samples for scale=4% and 10% reserved for evaluation for scale=8.

**Model evaluation and transfer learning:** Cave dataset is used for evaluating and tuning the model to facilitate the adaptability and strength of the image super-resolution workflow across various hyperspectral image datasets (Figure 2).

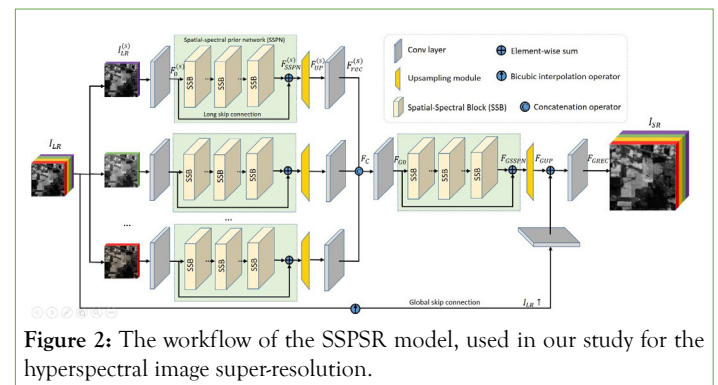


**Figure 2:** The workflow of the SSPSR model, used in our study for the hyperspectral image super-resolution.

### Overview and structure

The SSPSR model is structured into two core segments to process hyperspectral images effectively. The first segment comprises branch networks, which are specialized to manage distinct spectral bands or features through a sequential process: Initially performing shallow feature extraction, followed by deep spatial-spectral feature extraction. These initial steps are important for isolating and enhancing relevant spatial and spectral characteristics. The second segment is the global network, where the refined features from each branch are up scaled through an up sampling module and then integrated to reconstruct the high-resolution hyperspectral image, ensuring both detailed spatial representation and spectral integrity are preserved.

**Shallow and deep feature extraction:** In the SSPSR model's initial stage, patterns within hyperspectral images are identified through initial convolutional layers. The process progresses to a more advanced stage, known as the spatial-spectral deep feature extraction segment, where the model uses deeper convolutional layers combined with nonlinear activations to extract and enhance complex features and discern subtle interplay between spatial detail and spectral information within the data.

**Up sampling and reconstruction:** The up sampling module elevates the resolution of these features, preparing them for the final reconstruction phase. The latter, often comprising several convolutional layers, refines and transforms the up scaled features into coherent, detailed, higher-resolution images.

**Handling spectral bands:** Progressive up sampling by a factor of 2 and spectral grouping are used to manage the high dimensionality of spectral bands and reduce parameters. Efficient residual learning and attention mechanisms are leveraged to exploit spatial-spectral features effectively (Figure 3).

### Branch architecture

The branch networks commence with a Conv2d layer, followed by a SSPN that includes three Spatial-Spectral Blocks (SSB) featuring ResBlocks and ResAttentionBlocks. The attention mechanism is realized through a Channel Attention (CA) layer, focusing on the most informative features. The trunk network mirrors the branch's structure, enhanced with a skip convolutional layer for refined feature processing. The architecture concludes with a final convolutional layer, utilizing over 8 million trainable parameters, showcasing its capability to learn complex spatial-spectral patterns.

Each SSB uses ResBlocks and ResAttentionBlocks, integrating convolutional layers and a CA layer to heighten the focus on significant features. An up sampler in the final SSB, utilizing a PixelShuffle operation, facilitates the creation of super-resolved images with enriched spatial resolution. The SSPSR model, with its intricate design and integration of advanced techniques like residual learning and attention mechanisms, underscores its capability to deliver superior performance in the spatial and spectral domains. Each layer and block are meticulously crafted to extract, process and enhance features, promising detailed and accurate super-resolved hyperspectral images (Figure 4).

### Data pre-processing (Chikusei)

The Chikusei hyperspectral dataset, acquired using the Headwall Hyperspec-VNIR-C imaging sensor, covers agricultural and urban areas in Chikusei, Ibaraki, Japan. This dataset includes 128 bands spanning the spectral range of 363 nm to 1018 nm as shown in Figure 4.

We began pre-processing by cropping the central region of the

hyperspectral image to produce a sub-image of 2304 x 2048 x 128 pixels. This sub-image was divided into two sets:

**Testing dataset:** The upper portion, comprising four non-overlapping hyperspectral images with dimensions of 512 x 512 x 128 pixels.

**Training dataset:** Depending on the up sampling factor (scale), sub-images were extracted at either 64 x 64 pixels with a 32-pixel overlap for scale=4, or 128 x 128 pixels with a 64-pixel overlap for scale=8. To generate low-resolution hyperspectral images, Bicubic Interpolation was used. This technique used a 4 x 4 grid of neighboring pixels and a weighted averaging method to estimate pixel values at non-grid positions. The generated images for scale=4 included ms (16 x 16), ms\_bicubic (64 x 64) and gt (64 x 64), while for scale=8, the images included ms (32 x 32), ms\_bicubic (128 x 128) and gt (128 x 128). The entire process resulted in two distinct datasets, each with 3,700 samples: One for scale=4 and another for scale=8. For both scales, 10% of the samples were reserved for evaluation. This figure illustrates the spatial and spectral resolution of the hyperspectral image and its importance in the analysis.

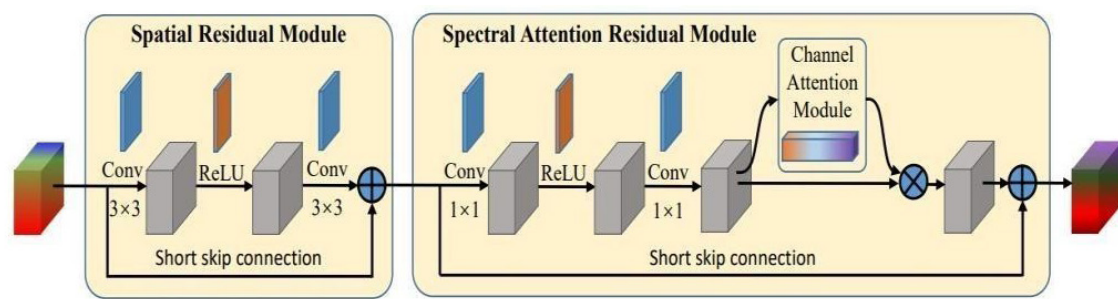


**Figure 3:** The architecture of a Spatial-Spectral Block (SSB) within the SSPSR model, depicting the flow from the spatial residual module through to the spectral attention residual module.



**Figure 4:** Chikusei hyperspectral image, captured by the Headwall Hyperspec-VNIR-C imaging sensor.

## Evaluation measures for image super resolution

In our project, we used the following six quantitative measures known as Performance Quality Indices (PQI) on the test dataset to rigorously assess the performance of our proposed hyperspectral image super-resolution method. The image reconstructed at a high resolution was compared against the ground-truth image using these measures.

**Cross-Correlation (CC):** CC is used to measure the degree of linear association between the reconstructed hyperspectral images and the corresponding ground truth data. Cross-correlation helps quantify image similarity by measuring how well one image “slides” over another image results in matching intensity patterns. It essentially calculates how much the pixel intensities of two images overlap at different positions. A high correlation value indicates a good overlap, suggesting the images are similar. A higher CC value indicates a stronger alignment and similarity between the images.

$$CC = \frac{\sum y g_t}{\sqrt{\sum y^2} \sqrt{\sum g_t^2}}$$

where  $y$  is the image reconstructed at high resolution;  $g_t$  is ground-truth image. While cross-correlation is a common tool for image similarity, it is limited by noise and with rotations, scaling, distortion, deformation, or lighting changes between the images. This is because it relies heavily on exact pixel values. For more strong similarity measures, consider methods like SSIM which look at patterns, Histogram of Oriented Gradient (HOG) which focuses on gradients, or Scale-Invariant Feature Transform (SIFT) which identifies key features-all offering some level of invariance to common image variations.

**Spectral Angle Mapper (SAM):** SAM quantifies the spectral similarity between two hyperspectral images by calculating the angular difference between their spectral vectors. Unlike cross-correlation which focuses on pixel intensity values, SAM analyses the spectral signature of each pixel, which provides a more comprehensive understanding of the material composition. A lower SAM value signifies a greater level of spectral similarity. A smaller SAM indicates a higher degree of similarity between the spectral signatures of the pixels, suggesting they likely represent the same material.

$$SAM = \arccos \left( \frac{\sum y g_t}{\sqrt{\sum y^2} \sqrt{\sum g_t^2}} \right)$$

SAM enhances the spectral information, making it more strong to variations in lighting or illumination compared to methods based on intensity values alone. The spectral angle has a physical meaning, relating directly to the spectral characteristics of the materials. Calculating the spectral angle for every pixel in an image can be computationally expensive for large datasets. While methods like cross correlation rely on intensity values, SAM provides a more material-specific perspective. This makes it valuable in situations where lighting variations might affect intensity but not necessarily the underlying spectral properties of the materials.

**Root Mean Squared Error (RMSE):** RMSE serves as a measure of the average magnitude of the differences between corresponding pixel values in the reconstructed and ground-truth images. A lower RMSE value indicates smaller differences and a higher degree of image-reconstruction fidelity. RMSE calculates the average squared difference between corresponding pixels in two images. A

lower RMSE indicates a smaller average difference, but it doesn't necessarily translate to higher image similarity.

$$RMSE = \sqrt{\frac{\sum (y - g_t)^2}{N}}$$

Where N is number of pixels. While Root Mean Squared Error (RMSE) calculates average intensity differences between images, it's not ideal for direct similarity assessment. Images with similar structures but different lighting or noise can have a high RMSE despite being visually similar. RMSE can be a helpful tool alongside other techniques, but for a stronger measure, consider methods like SSIM which analyse structural information or feature-based approaches that identify key point features for matching. In tasks like image super-resolution where you're trying to reconstruct a higher resolution image from a lower resolution one, RMSE can be used as a basic metric to compare the reconstructed image's pixel intensities to the ground truth (original high-resolution image).

**Erreur Relative Globale Adimensionnelle de Synthèse (ERGAS):** ERGAS is a commonly used evaluation measure in the field of image processing and remote sensing, particularly for assessing the performance of super-resolution algorithms applied to hyperspectral images. It takes into account both spatial and spectral fidelity of the reconstructed image. A lower ERGAS score indicates better performance, indicating that reconstructed image closely resembles the original high-resolution image.

ERGAS evaluates image super-resolution by calculating the Mean Squared Error (MSE) between original and reconstructed images, assessing pixel-wise differences, for each band. It incorporates a scaling factor to adjust for variations in image variability and a global factor to normalize errors across the entire image, preventing bias towards specific regions. ERGAS synthesizes these elements into a dimensionless metric, offering a relative measure of error independent of image scale or units. ERGAS provides a single, dimensionless score between 0 and 100.

$$ERGAS = 100 \times \sqrt{\left( \frac{1}{M} \right) \sum \left( \frac{(y - g_t)^2}{g_t^2} \right)}$$

Where M is the number of bands. Lower ERGAS values correspond to superior performance. It provides a dimensionless metric, allowing for easy comparison across different datasets and scales. ERGAS is advantageous when assessing the performance of algorithms that aim to improve both spatial and spectral resolution simultaneously. Unlike ERGAS, SAM is useful when the primary concern is the spectral accuracy of the reconstructed image rather than spatial details.

**Peak Signal-to-Noise Ratio (PSNR):** PSNR is a widely used metric for quantifying the quality of reconstructed or enhanced images, including those produced by super-resolution algorithms. It computes the ratio between the maximum possible power of the original signal and the power of the noise that affects the fidelity of the reconstruction. A higher PSNR value signifies better image quality.

$$PSNR = 10 \times \log_{10} \left( \frac{Max^2}{MSE^2} \right)$$

Where Max is the maximum possible pixel value. PSNR evaluates image reconstruction quality by first computing the MSE between

the original and reconstructed images, measuring the average squared difference between corresponding pixels. It then normalizes the MSE by dividing the maximum possible pixel value squared by the MSE to ensure relative assessment. Applying a logarithmic transformation enhances PSNR's sensitivity to subtle differences and scaling the result by 10 provides the PSNR value in decibels, a standard unit for expressing signal-to-noise ratios.

PSNR lacks sensitivity to perceptual differences and structural distortions, focusing solely on pixel-wise errors. Additionally, PSNR's dependence on image content and insensitivity to spectral fidelity make it less suitable for tasks where preserving perceptual and spectral quality is important. For example, images with high levels of detail or texture may exhibit lower PSNR values even if they are visually pleasing. PSNR assumes a fixed dynamic range for all images, which may not be suitable for datasets with varying dynamic ranges or different bit depths.

**Structural Similarity Index (SSIM):** SSIM measures the structural similarity between the reconstructed and reference original hyperspectral images, considering factors such as luminance, contrast and structure. The Structural Similarity Index (SSIM) goes beyond pixel-by-pixel intensity differences and offers a more comprehensive measure to quantify the performance of image super-resolution techniques. A higher SSIM value indicates greater structural similarity and higher image quality.

$$SSIM = \frac{(2\mu_y\mu_{gt} + C_1)(2\sigma_{yg} + C_2)}{(\mu_y^2 + \mu_{gt}^2 + C_1)(\sigma_y^2 + \sigma_{gt}^2 + C_2)}$$

Where  $\mu_y$ ,  $\mu_{gt}$  are mean,  $\sigma_y$ ,  $\sigma_{gt}$  are standard deviation,  $\sigma_{yg}$  is covariance of  $y$  and  $gt$  and  $C_1$ ,  $C_2$  are small constants for stability.

SSIM computes the metric as a product of three comparisons: luminance (mean) comparison, contrast (variance) comparison and structural (covariance) comparison. The SSIM score ranges between -1 and 1, where 1 indicates perfect similarity between the images. Higher SSIM values suggest higher perceptual similarity and better image quality. Its performance can vary depending on the content of the images being compared and may not handle scaling or translation differences effectively. SSIM may also lack sensitivity to high-frequency details and compression artefacts, limiting its applicability in certain scenarios. Additionally, SSIM's complexity and subjectivity in parameter selection pose challenges and it should be used alongside other metrics and subjective evaluations for a comprehensive assessment of image quality.

SSIM, while effective in measuring structural similarity, lacks in assessing spectral fidelity compared to metrics like SAM or ERGAS, which excel in remote sensing and hyperspectral imaging applications.

**Table 1:** Comparative performance metrics of SSPSR model approaches. This table enumerates the outcomes of various super-resolution approaches against the benchmark SSPSR paper results, showcasing the balance between model accuracy, as reflected by MPSNR and MSSIM and efficiency, as denoted by Time/Epoch.

Model	MPSNR	MSSIM	ERGAS	SAM	Cross correlation	RMSE	Time/Epoch
SSPSR paper results	40.361 2	0.941 3	4.9894	2.353	0.9565	0.0114	NA
Approach 1: Evaluation with full dataset replication	40.334 2	0.943 6	4.9563	2.377	0.95643	0.0115	600 sec
Approach 2: Spectral prioritization for super-resolution	39.647 7	0.936 0	5.3932	2.64	0.9491	0.0123	240 sec
Approach 3: Prioritizing bands with high PSNR	39.182 6	0.931 7	5.7464	2.865	0.9435	0.0129	300 sec

Additionally, SSIM's sensitivity to image content variations and its computational complexity may limit its applicability in scenarios where strong spectral assessment or computational efficiency is important. Therefore, SAM and ERGAS may offer advantages in such contexts.

One advantage of SSIM over SAM and ERGAS in image super-resolution is its ability to consider local structural information, luminance and contrast, which align more closely with human perception of image quality. This holistic approach enables SSIM to capture subtle details and textures, making it effective in assessing perceptual similarity between the original and super-resolved images. Additionally, SSIM's computational efficiency and simplicity compared to SAM and ERGAS make it more practical for real-time applications or large-scale image processing tasks. Additionally, SSIM's capability to handle scaling and translation differences more effectively compared to PSNR makes it more suitable for evaluating the quality of super-resolved images that undergo geometric transformations.

The best possible values for these indices are defined as follows: 1 for CC and SSIM, 0 for SAM, RMSE and ERGAS and  $+\infty$  for PSNR. The min and max values for each metric are as follows: CC (0 to 1), SAM (0 to  $\infty$ ), RMSE (0 to  $\infty$ ), ERGAS (0 to  $\infty$ ), PSNR (0 to  $\infty$ ), SSIM (0 to 1).

## RESULTS AND DISCUSSION

The study is centered around the overarching goal of reducing computation time while optimizing the super-resolution of hyperspectral images. To achieve this, we explored various approaches and compared their outcomes to the results from a referenced research paper [19]:

### Approach 1: Evaluation with full dataset replication

As a part of our extensive assessment, we undertook an experiment encompassing the entire dataset, comprising 3,700 samples. The objective was to faithfully reproduce the parameters and configurations closer to SSPSR paper results by Jiang et al., (Table 1), thereby subjecting our method to a rigorous validation process [19]. The experimental setup entailed 40 training epochs, batch size of 32 with an initial learning rate of  $1e-4$  which decays by a factor of 10 when it reaches 30 epochs, the deployment of 8 groups for super-resolution and the inclusion of 2-band overlap sections, meticulously mirroring the parameters specified in the reference SSPSR paper. Our results harmoniously converged with the parameters and outcomes articulated in the paper, consolidating our confidence in the effectiveness of our approach. This alignment provides a strong foundation for future exploration and fine-tuning in the pursuit of hyperspectral image super-resolution.

### Approach 2: Spectral prioritization for super-resolution

Our approach drew inspiration from the paper's emphasis on leveraging spectral information for super resolution. We sought to prioritize spectral bands with mean values exceeding 0.1. The rationale behind this approach was to exploit the wealth of distinctive spectral information that brighter regions contained within the hyperspectral data. This allowed us to focus on 700 out of 3000 training samples, significantly narrowing down the computational load to 240 sec/epoch. However, some discrepancies emerged in the results, notably in the SSIM and PSNR metrics. Additionally, reducing the training sample size could be considered a drawback, highlighting the challenge of working with limited data in hyperspectral image super-resolution tasks.

### Approach 3: Prioritizing bands with high PSNR

We aimed to optimize computational efficiency while maintaining high-quality super resolution. We accomplished this by selecting spectral bands with PSNR values surpassing 40 for prioritized super resolution, which led to a reduced set of 650 training samples, down from the original 3,000. This approach resulted in a remarkable reduction in training time, with 300 sec/epoch. However, a closer examination of the outcomes uncovered minor disparities, notably in the PSNR, SAM, ERGAS and SSIM metrics. Furthermore, while this criterion seemed promising in theory, it didn't yield the

expected results in practice. The high PSNR bands were limited and the downsizing of the training dataset introduced challenges, such as overfitting, as the model had to generalize from a smaller and potentially biased sample. These insights underscored the intricate trade-off between computational efficiency and image quality preservation, offering valuable insights for the next approach.

### Approach 4: Efficient band selection

The bands were selected based on their mean values and spectral characteristics. For 8 bands, the selected wavelengths were 450 nm, 500 nm, 550 nm, 600 nm, 650 nm, 700 nm, 750 nm and 800 nm. In our fourth approach, we selectively trained the model on hyperspectral data with varying band counts, ranging from 8, 16, 32, 64 to 128 bands. The results are presented in Table 2. The primary objective was to pinpoint the optimal trade-off that would lead to the most efficient yet high-quality super-resolution results without reducing training sample size. After training our model using the above approach, the results produced by the trained models were enlightening. In the comparison below, we present the ground truth image, the original low-resolution (compressed) training image and the reconstructed output images generated by models trained with 8, 16, 32, 64 and 128 bands, respectively. The images encapsulate the journey from low-resolution to high-resolution, highlighting the potential of hyperspectral image super-resolution (Figure 5).

**Table 2:** Efficiency and effectiveness of 8-band model in hyperspectral image super-resolution. This table presents the performance metrics of models trained with different numbers of spectral bands, highlighting the balance between computational efficiency and image quality.

No. of channels	MPSNR	MSSIM	ERGAS	SAM	Cross correlation	RMSE	Time/Epoch
128	40.3612	0.9413	4.9894	2.3527	0.9565	0.0114	600 sec
64	40.2946	0.9433	4.9774	2.4083	0.9561	0.0115	180 sec
32	40.3262	0.9434	5.1336	2.3719	0.9547	0.0115	120 sec
16	40.2565	0.9423	5.486	2.4046	0.9503	0.0116	80 sec
8	40.3096	0.9419	6.0014	2.4311	0.9439	0.0116	55 sec

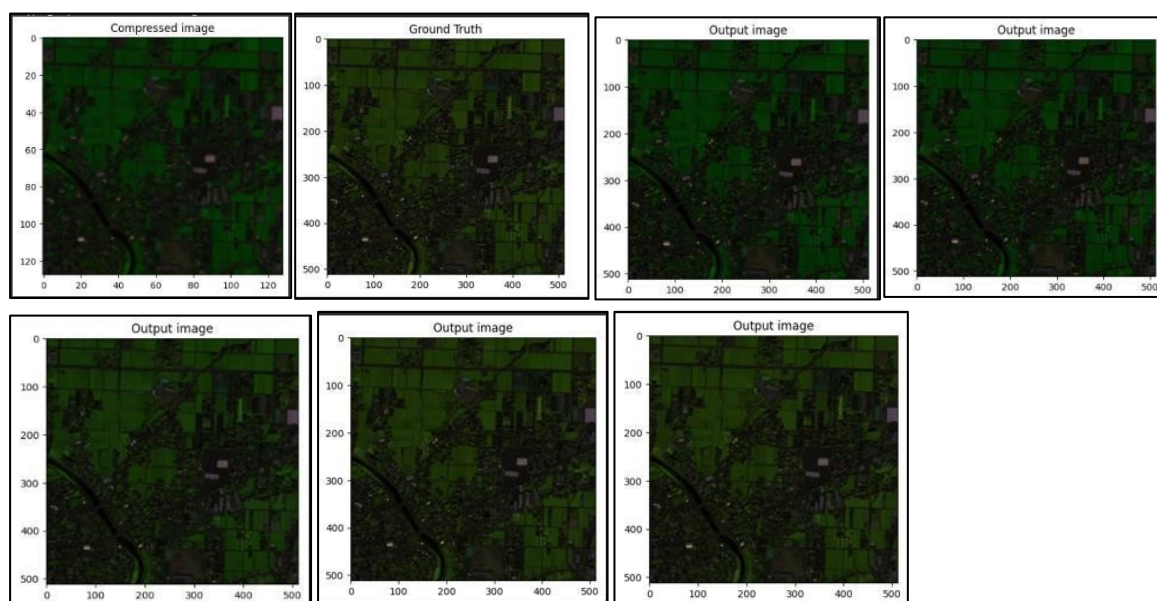


**Figure 5:** A progression of image resolutions, featuring the ground truth image, an original low-resolution (compressed) training image and reconstructed images produced by models trained with 8, 16, 32, 64 and 128 bands respectively.

To our surprise, we found that models trained with only 8 bands produced results that were remarkably close to those trained with a more extensive set of bands. Notably, this approach considerably improved computation efficiency, reducing the time per epoch to just 55 sec. While there were slight variations in PSNR and SSIM metrics, the efficiency gains made this approach an appealing choice for hyperspectral image super-resolution objective.

In conclusion, after assessing various approaches to optimize hyperspectral image super-resolution, we have chosen to finalize our focus on the 8-band model for refining loss functions and further hyper parameter tuning. The first approach validated our method, aligning our results with paper results (Table 1). However, the second and third approaches, emphasizing spectral prioritization and high PSNR bands, highlighted challenges in balancing computational efficiency and image quality with limited data. The last approach demonstrated the efficiency of the 8-band model, producing outcomes closely comparable to models with more bands. Despite slight variations in metrics, the 8-band model significantly reduced computation time to 55 sec/epoch, making it an agreeable choice. Our decision of 8-band model reflects a strategic compromise between computational efficiency and high-quality super resolution, aligning with our project's goal of reducing processing time while maintaining satisfactory performance.

### Loss function

The original SSPSR deep-learning model utilizes a dual-component loss function (L1+TV) for hyperspectral image super-resolution. However, a thorough assessment of the SSPSR model outcomes indicates the need for refinement of the loss function to improve fidelity and perceptual quality. To address these limitations, a new loss function was incorporated. The integration of SAM and SSIM in the new loss function established a multifaceted optimization approach, effectively balancing pixel accuracy, spatial smoothness, spectral fidelity and perceptual quality.

**Fidelity loss (L1):** Measures absolute differences between predicted and actual pixel values, ensuring precise reconstruction while being strong to outliers.

$$L1(y, gt) = \frac{\sum_{i=1}^N |y_i - gt_i|}{N}$$

Where  $y$  is reconstructed and  $gt$  is ground truth vectors; N is number of pixels.

**Total Variation loss (TV):** Promotes spatial and spectral smoothness, minimizing noise while preserving image details.

$$TV(y, gt) = \sum_{i,j=1}^N \sqrt{(y\{i+1, j\} - gt\{i, j\})^2 + (y\{i, j+1\} - gt\{i, j\})^2}$$

Where  $y$  is reconstructed;  $gt$  is ground truth pixel vectors at locations in the x and y directions

**Spectral Angle Mapper loss (SAM):** Ensures spectral similarity for material identification and classification; provides a scale-invariant angle measurement. SAM was described in the previous section.

$$SAM(y, gt) = \cos^{-1} \left( \frac{\sum_{i=1}^N y_i * gt_i}{\|y\|_2 * \|gt\|_2} \right)$$

Where  $y$  is reconstructed and  $gt$  is ground truth vectors; N is

number of pixels; and  $\| \cdot \|_2$  are the L2 norms of the reconstructed and ground truth vectors, respectively.

**Structural Similarity Index Measure loss (SSIM):** Preserves structural integrity in reconstructed hyperspectral images; provides a perceptually relevant measure of image quality. This metric has been explained in the previous section.

In the subsequent section, we will delve into the tuning process for the hyper parameters ( $\alpha, \beta, \gamma, \delta$ ) of the new loss function, ensuring optimal performance and adaptability across diverse hyperspectral image super-resolution scenarios. These hyper parameters govern the relative weightage and importance of each loss term in the overall loss function containing 4 distinct terms.

### Hyper parameter tuning

In our exhaustive exploration of hyper parameter tuning for the SSPSR model, we observed intricate dynamics between the loss function weights ( $\alpha, \beta, \gamma, \delta$ ) and the overall model performance. The results in Table 3, shed light on the delicate balance required to prevent overfitting and model divergence while achieving optimal hyperspectral image super-resolution.

For the optimization process, we focused on the hyper parameter alpha ( $\alpha$ ), which scales the L1 loss, also known as fidelity loss, in the model's loss function. By adjusting alpha, we were able to control the importance of pixel-wise accuracy in the model's training objective. A higher alpha value placed greater emphasis on minimizing these differences, thereby prioritizing fidelity in the super-resolution process. However, we observed that as alpha was reduced beyond a certain threshold, specifically below 0.1, the model began to struggle with generalization, leading to an overfitting issue. Overfitting was particularly noticeable when the fidelity loss was weighted too heavily ( $\alpha > 1$ ), causing a neglect of other critical aspects such as image smoothness and spectral fidelity, which ultimately diminished the model's performance on the test data.

Conversely, the total variation loss hyper parameter ( $\beta$ ), responsible for promoting spatial and spectral smoothness, demonstrated a similar sensitivity. Lower values ( $\beta < 0.001$ ) compromised the model's ability to reduce noise and preserve image details, negatively impacting performance metrics. However, overly emphasizing smoothness with higher  $\beta$  ( $\beta > 1$ ) values led to model divergence, as the optimization process favoured overly simplistic reconstructions, lacking sufficient detail and fidelity.

The SAM loss ( $\gamma$ ) and SSIM loss ( $\delta$ ) played pivotal roles in preserving spectral and structural features. We found that lower values of  $\gamma$  and  $\delta$  ( $\gamma, \delta < 0.01$ ) resulted in diminished spectral similarity and structural integrity, leading to suboptimal super resolution. On the other hand, excessively high values ( $\gamma, \delta > 1$ ) caused divergence, as the model struggled to strike a balance between accuracy and smoothness.

Notably, the best-performing set of hyper parameters ( $\alpha=0.1, \beta=0.001, \gamma=0.01, \delta=0.01$ ) struck a harmonious equilibrium. This combination allowed for pixel-wise accuracy, smoothness, spectral fidelity and structural integrity, contributing to the highest MPSNR and MSSIM values. ( $\alpha=0.1, \beta=0.001, \gamma=0.01, \delta=0.01$ )

The metrics MPSNR, MSSIM, ERGAS, SAM, Cross Correlation and RMSE are utilized to evaluate image super-resolution quality.

MPSNR and MSSIM measure signal quality and structural similarity, respectively, with higher values indicating better fidelity to the original image. ERGAS assesses the relative error and lower values represent a more accurate reconstruction. SAM compares the angle between spectral data vectors, with smaller angles suggesting higher spectral accuracy. Cross Correlation examines the linear relationship between the predicted and reference images, where higher values mean better correlation. RMSE calculates the standard deviation of prediction errors, with lower values denoting

higher predictive accuracy. Together, these indices provide a comprehensive evaluation of the spatial and spectral quality of the super-resolved images.

The results below in Table 3, underline the nuanced interaction of hyper parameters in achieving optimal performance and the findings from this tuning process provide valuable insights into crafting a well-balanced SSPSR model for hyperspectral image super-resolution; with the best combination highlighted.

**Table 3:** Hyper parameter tuning of loss function weights for 8-band hyperspectral image. Best performance is at the top of the list.

Alpha ( $\alpha$ )	Beta ( $\beta$ )	Gamma ( $\gamma$ )	Delta ( $\delta$ )	MPSNR	MSSIM	ERGAS	SAM	Cross correlation	RMSE
1	1	0	0	40.4	0.941	4.99	2.35	0.957	0.011
1	1	1	1	39.8	0.932	7.37	2.71	0.92	0.0129
1	1	2	2	38.6	0.922	9.59	5.77	0.908	0.0178
1	0.1	0.1	0.1	40.6	0.942	6.88	2.52	0.931	0.0117
1	1	0.01	0.01	40.5	0.941	6.96	2.6	0.929	0.0119
1	0.1	0.01	0.01	40.8	0.944	6.82	2.47	0.932	0.0115
1	0.1	0.05	0.05	40.7	0.942	6.85	2.54	0.931	0.0117
1	0.1	0.01	0.001	40.7	0.943	6.84	2.53	0.931	0.0116
1	0.1	0.001	0.01	40.5	0.941	6.91	2.6	0.93	0.0119
1	0.1	0.001	0.001	40.7	0.943	6.86	2.56	0.931	0.117
1	0.1	0.00001	0.00001	40.3	0.942	4.78	2.42	0.924	0.116
1	1	0.01	0.01	40.5	0.941	6.96	2.6	0.929	0.0118
1	2	0.01	0.01	38.6	0.931	9.39	5.57	0.918	0.0166
1	3	0.01	0.01	37.4	0.916	11.9	7.43	0.902	0.0205
2	1	0.01	0.01	36.5	0.911	10.6	4.74	0.903	0.0197
1	0.01	0.01	0.01	40.7	0.944	6.83	2.49	0.931	0.0116
1	0.001	0.01	0.01	40.7	0.943	6.83	2.48	0.931	0.0115
0.1	0.001	0.01	0.01	40.7	0.949	6.81	2.48	0.931	0.0115
0.001	0.001	0.01	0.01	40.2	0.937	7.08	2.51	0.925	0.0124
0.0001	0.0001	0.01	0.01	38.4	0.923	8.39	2.52	0.907	0.0149

## Modification of architecture with tuned loss function weights

In the pursuit of enhancing the capabilities of the SSPSR model, modifications were introduced to its architecture, specifically targeting the number of spatial-spectral blocks and filters. The objective was to strike a delicate balance between computational efficiency, model complexity and the preservation of spectral and spatial information intrinsic to hyperspectral data. The SSB serve to partition the spectral data into manageable segments, thereby facilitating the extraction of intricate spatial and spectral features. Filters, on the other hand, refer to the convolutional kernels used within these blocks to process the data. The augmentation of SSB branches, as described in the Model and Branch Architecture section, aimed to bolster the model's proficiency in extracting these features, while variations in the number of filters were implemented to assess their impact on information flow within the network.

In this experiment, the hyper parameters tuned included the number of SSB branches and the number of filters per block. Adjusting the number of blocks allows for better handling of

the spectral data's complexity, while varying the filters helps optimize the model's ability to capture detailed spectral and spatial information. Specifically, we experimented with different configurations of blocks and filters to evaluate their effects on the model's performance. The results presented in Table 4, illustrate the performance of the modified architectures compared to the baseline, considering both Scale=4 and Scale=8.

In summary, the exploration of refined architectures offers valuable insights into the intricate interplay of model parameters and their ramifications on hyperspectral image super-resolution. In Scale=4 and Scale=8 super-resolution experiments, performance improved with an increase in blocks, peaking at 3 blocks, with 256 features. However, fewer features, like 16 and more blocks like 7 resulted in performance decline across metrics. Optimal outcomes materialize with a configuration using three blocks, each housing 256 features. These findings emphasize the necessity for a customized approach in designing hyperspectral image super-resolution models, recognizing the distinct challenges presented by the high-dimensional nature of spectral data.

**Table 4:** Hyper parameter tuning of model architecture for 8-band model in hyperspectral image super-resolution for scale 4 and scale 8 super-resolution of the hyperspectral images in the Chikusei Dataset. Best performance is highlighted.

Scale=4							
Scale	Parameters	MPSNR	MSSIM	ERGAS	SAM	Cross correlation	RMSE
4	SSPSR	40.4	0.941	4.98	2.352	0.956	0.0114
4	1 block, 256 features	40.5	0.938	6.96	2.59	0.928	0.012
4	3 blocks, 16 features	39.3	0.921	7.71	3.094	0.911	0.0137
4	3 blocks, 64 features	40.1	0.934	7.15	2.703	0.923	0.0124
4	3 blocks, 256 features	40.8	0.943	6.81	2.48	0.931	0.0115
4	3 blocks, 512 features	40.3	0.936	7.19	2.679	0.927	0.012
4	5 blocks, 256 features	40.8	0.943	6.81	2.495	0.931	0.0115
4	7 blocks, 256 features	40.7	0.942	6.9	2.534	0.931	0.0116
Scale=8							
8	SSPSR	35.8	0.862	4.31	4.01	0.877	0.019
8	1 block, 256 features	36.7	0.857	9.64	4.17	0.849	0.019
8	3 blocks, 16 features	35.9	0.837	10.3	4.67	0.825	0.021
8	3 blocks, 64 features	36.5	0.854	9.78	4.26	0.845	0.019
8	3 blocks, 256 features	36.8	0.862	9.58	4.06	0.853	0.019
8	3 blocks, 512 features	36.6	0.856	9.75	4.28	0.848	0.019
8	5 blocks, 256 features	36.8	0.863	9.53	4.06	0.853	0.019
8	7 blocks, 256 features	36.8	0.863	9.59	4.08	0.852	0.019

### Model architecture and performance comparison for scale=4 and scale=8

This section undertakes a comprehensive examination of the architectural differences between two hyperspectral image super-resolution models, optimized for Scale=4 and Scale=8. The comparison between Scale=4 and Scale=8 is made in Table 5. These models were configured with a tuned loss function and the optimal setup obtained (in the above results), involved 3 blocks and 256 features. The differences in specific layers and parameters significantly influence their ability to process hyperspectral data at different upscaling factors. Notable differences include the shapes of layer parameters within the up sample, trunk and branch structures of SSB (described in Branch and Model Architecture section). This is because, for Scale=8, a larger parameter space (range of possible values for the hyper parameters of the SSPSR model being

optimized) is needed to capture and process more complex features and patterns in the data. Despite these differences, global branch layers maintain consistent parameters across both scales, ensuring the stability of shared model features and efficient parameter sharing. (number of filters or neurons).

A quantitative assessment of each model's performance is summarized in Table 5. While the increased parameter space for Scale=8 allowed for a higher resolution, it resulted in higher errors, as indicated by elevated RMSE and SAM values. The lower MPSNR and MSSIM values also suggest a potential sacrifice in terms of image quality. In contrast, the Scale=4 model with lower resolution exhibited better quantitative metrics, indicating lower errors and higher image quality. The results highlight the inherent trade-off between higher resolution scaling and model accuracy (number of filters or neurons) (Figures 6 and 7).

**Table 5:** Hyperspectral image super-resolution performance metrics for different scales.

Scale	MPSNR	MSSIM	ERGAS	SAM	Cross correlation	RMSE
4	40.4	0.941	4.99	2.35	0.956	0.011
8	35.8	0.862	4.31	4.01	0.877	0.019

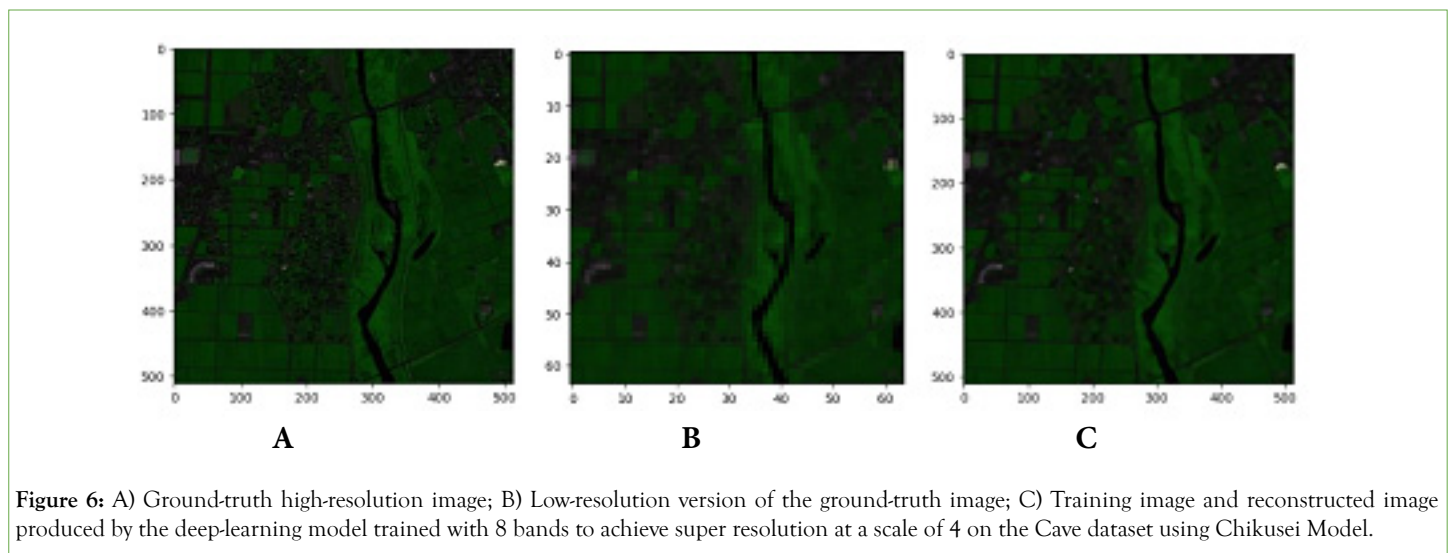


**Figure 6:** A) Ground-truth high-resolution image; B) Low-resolution version of the ground-truth image; C) Training image and reconstructed image produced by the deep-learning model trained with 8 bands to achieve super resolution at a scale of 4 on the Cave dataset using Chikusei Model.

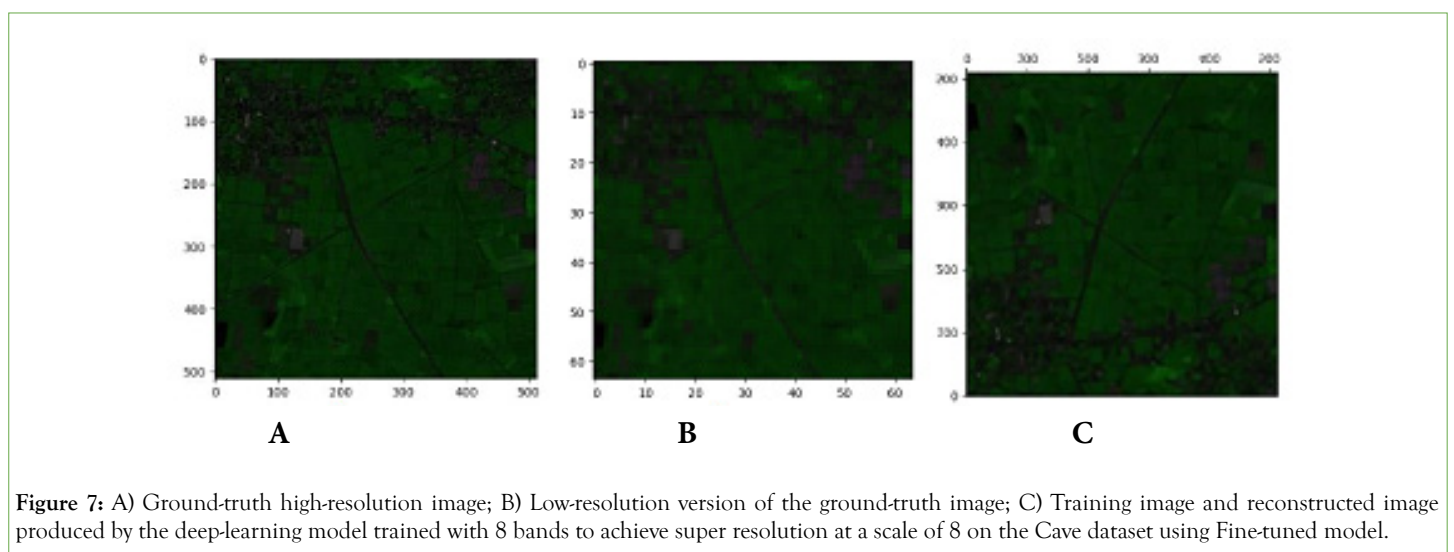


**Figure 7:** A) Ground-truth high-resolution image; B) Low-resolution version of the ground-truth image; C) Training image and reconstructed image produced by the deep-learning model trained with 8 bands to achieve super resolution at a scale of 8 on the Cave dataset using Fine-tuned model.

### Data pre-processing (CAVE)

The Cave dataset is a multispectral image dataset that comprises 32 scenes of everyday objects with spatial dimensions of 512 x 512 and 31 spectral bands ranging from 400 nm to 700 nm at 10 nm intervals. For training, 20 hyperspectral images were randomly selected, with 2 reserved for evaluation. Patches of 64 x 64 pixels (32 pixels' overlap) were used for up sampling factor  $d=4$ . For up sampling factor of  $d=8$ , patches of 128 x 128 pixels (with 64 pixels' overlap) were used. Bicubic down-sampling generated low-resolution hyperspectral images with factors of 4 or 8. The remaining 12 hyperspectral images were allocated for testing, treating the originals as ground truth.

### Fine tuning

Our final Chikusei model (fine-tuned), is characterized by its trained weights, utilization of 8 spectral bands and architecture comprising 3 blocks with 256 features each. This model was trained on the Chikusei dataset to enhance its performance and accuracy in processing high-dimensional spectral data. To assess the generalizability of the model, we evaluated its deployment performance on the Cave dataset. This evaluation aimed to

determine whether a model trained on airborne agricultural and urban scenes could effectively classify objects in a different hyperspectral dataset. Furthermore, we explored the potential of fine-tuning on a new dataset (Cave), to ascertain if the fine-tuning could improve the super-resolution performance.

The Chikusei model, Cave model and fine-tuned Chikusei model results are listed in Table 6. Cave model refers to training from scratch using Cave data. Chikusei model refers to the model trained on the Chikusei dataset. Fine-tuned Chikusei model refers to the model trained on the Chikusei dataset and then fine-tuned on the Cave dataset. The results use MPSNR and MSSIM for model comparisons as they are widely recognized metrics for assessing image quality and reconstruction accuracy. The results demonstrate that fine-tuning significantly improves the model's performance on the Cave dataset compared to training from scratch. The fine-tuned model outperforms the original model, suggesting that the additional training data provided by the Cave dataset allowed the model to learn more effectively. This finding highlights the potential of transfer learning for hyperspectral image classification tasks (Figures 8-10).

**Table 6:** Fine tuning results for the Cave dataset.

Scale	Dataset	Model name	MPSNR	MSSIM
4	Chikusei	Chikusei model	40.7	0.943
8	Chikusei	Chikusei model	36.8	0.862
4	Cave	Chikusei model	29.4	0.867
4	Cave	Fine-tuned model	30.5	0.913
4	Cave	Cave model	29.8	0.897
8	Cave	Chikusei model	28.5	0.793
8	Cave	Finer Tuned Chikusei model	29.9	0.864
8	Cave	Cave model	29.5	0.855

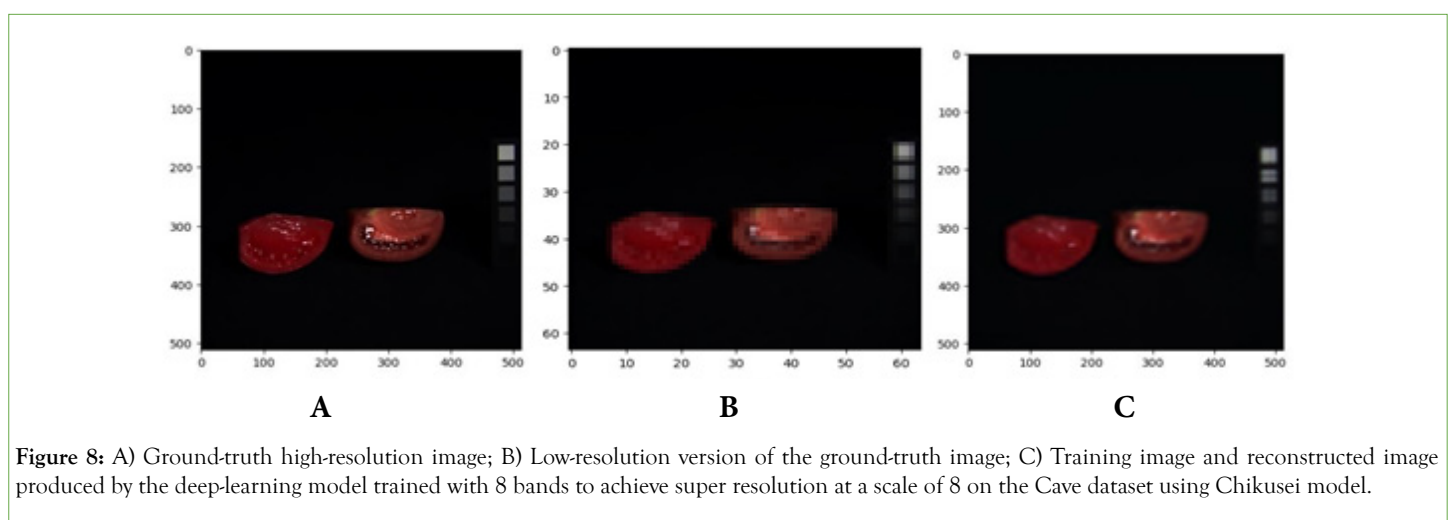


**Figure 8:** A) Ground-truth high-resolution image; B) Low-resolution version of the ground-truth image; C) Training image and reconstructed image produced by the deep-learning model trained with 8 bands to achieve super resolution at a scale of 8 on the Cave dataset using Chikusei model.

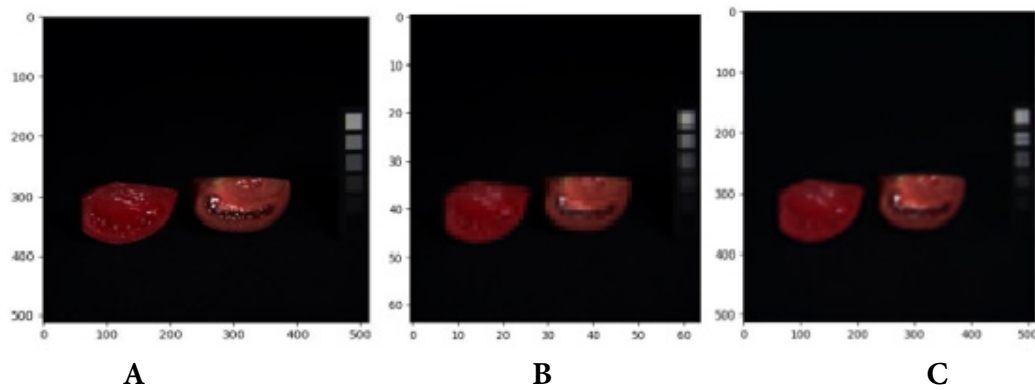


**Figure 9:** A) Ground-truth high-resolution image; B) Low-resolution version of the ground-truth image; C) Training image and reconstructed image produced by the deep-learning model trained with 8 bands to achieve super resolution at a scale of 8 on the Cave dataset using Fine-tuned model.

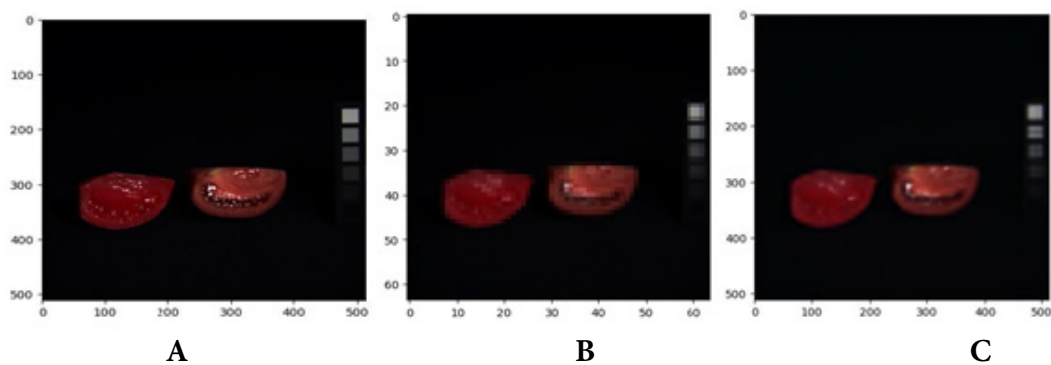


**Figure 10:** A) Ground-truth high-resolution image; B) Low-resolution version of the ground-truth image; C) Training image and reconstructed image produced by the deep-learning model trained with 8 bands to achieve super resolution at a scale of 8 on the Cave dataset using Cave model.

## CONCLUSION

The research successfully enhanced the spatial and spectral resolutions of hyperspectral images through the deployment of deep transfer learning. The utilization of the single-image super-resolution *via* a spatial-spectral prior model trained on the Chikusei dataset yielded commendable PQI metrics, showcasing its effectiveness in achieving significant improvements in enhancing the resolution. Furthermore, the study conducted rigorous hyper parameter tuning to identify the optimal model architecture, emphasizing the importance of fine-tuning in achieving superior results. The introduction of novel loss functions and the meticulous optimization of hyper parameters demonstrated a strategic approach to evaluating and enhancing the model's efficacy, particularly when dealing with 8band hyperspectral image input. A pivotal aspect of this research involved the comprehensive evaluation of the final fine-tuned model's performance, comparing its effectiveness in 4x and 8x image enhancement scenarios. This comprehensive analysis provided valuable insights into the versatility and adaptability of the developed model across varying degrees of image enhancement.

To validate the generalizability of the model, an assessment was conducted on the Cave dataset, affirming its strong performance even when applied to different datasets. The successful transition from the Chikusei to the Cave dataset underscores the model's adaptability and underscores its potential utility in diverse hyperspectral imaging applications. In summary, this research contributes significantly to the field by not only achieving successful enhancements in spatial and spectral resolution but also

by presenting a comprehensive framework for model optimization, evaluation and generalization. These findings are poised to advance the use of deep learning in hyperspectral image processing and pave the way for future innovations in remote sensing and land cover mapping applications.

## REFERENCES

1. Lu G, Fei B. Medical hyperspectral imaging: A review. *J Biomed Opt.* 2014;19(1):010901.
2. Kurz TH, Buckley SJ. A review of hyperspectral imaging in close range applications. *ISPRS.* 2016;41:865-870.
3. Bahalul E, Bronfeld A, Epshtein S, Saban Y, Karsenty A, Arieli Y, et al. Hyperspectral imaging camera using wavefront division interference. *Opt Lett.* 2016;41(5):938-941.
4. Peyghambari S, Zhang Y. Hyperspectral remote sensing in lithological mapping, mineral exploration and environmental geology: An updated review. *J Appl Remote Sens.* 2021;15(3):031501.
5. Kwan C. Remote sensing performance enhancement in hyperspectral images. *Sensors.* 2018;18(11):3598.
6. Fotiadou K, Tsagkatakis G, Tsakalides P. Spectral resolution enhancement of hyperspectral images *via* sparse representations. *Electronic Imaging.* 2016;28:1-6.
7. Ablin R, Sulochana CH. A survey of hyperspectral image classification in remote sensing. *IJARCCCE.* 2013;2(8):2986-3000.
8. Caponi M, Cox A, Misra S. Viscosity prediction using image processing and supervised learning. *Fuel.* 2023;339:127320.

9. Wu Y, Misra S, Sondergeld C, Curtis M, Jernigen J. Machine learning for locating organic matter and pores in scanning electron microscopy images of organic-rich shales. *Fuel*. 2019;253:662-676.
10. Misra S, Li H. Long short-term memory and variational autoencoder with convolutional neural networks for generating NMR T2 distributions. *IEEE Geosci Remote Sens Lett*. 2018;16(2):192-195.
11. Li X, Zhang L, You J. Domain transfer learning for hyperspectral image super-resolution. *Remote Sens*. 2019;11(6):694.
12. Wu Y, Misra S. Intelligent image segmentation for organic-rich shales using random forest, wavelet transform, and hessian matrix. *IEEE Geosci Remote Sens Lett*. 2019;17(7):1144-1147.
13. Yuan Y, Zheng X, Lu X. Hyperspectral image super resolution by transfer learning. *IEEE. J Sel Top Appl Earth Obs Remote Sens*. 2017;10(5):1963-1974.
14. Liu Z, Zheng Y, Han XH. Deep unsupervised fusion learning for hyperspectral image super resolution. *Sensors*. 2021;21(7):2348.
15. Li H, Misra S, He J. Neural network modeling of *in situ* fluid-filled pore size distributions in subsurface shale reservoirs under data constraints. *Neural computation*. 2020;32:3873-3885.
16. Huang Q, Li W, Hu T, Tao R. Hyperspectral image super-resolution using generative adversarial network and residual learning. *IEEE ICASSP*. 2019;3012-3016.
17. Zou C, Huang X. Hyperspectral image super-resolution combining with deep learning and spectral un-mixing. *Signal Process Image Commun*. 2020;84:115833.
18. Wang C, Liu Y, Bai X, Tang W, Lei P, Zhou J, et al. Deep residual convolutional neural network for hyperspectral image super-resolution. *ICIG*. 2017;370-380.
19. Jiang J, Sun H, Liu X, Ma J. Learning spatial-spectral prior for super-resolution of hyperspectral imagery. *IEEE Trans Comput Imaging*. 2020;6:1082-1096.
20. Tang Z, Xu Q, Wu P, Shi Z, Pan B. Feedback refined local-global network for super-resolution of hyperspectral imagery. *Remote Sens*. 2022;14(8):1944.
21. Yokoya N, Iwasaki A. Airborne hyperspectral data over Chikusei. *Tech Rep*. 2016;5(5):5.
22. Park JI, Lee MH, Grossberg MD, Nayar SK. Multispectral imaging using multiplexed illumination. *IEEE*. 2007;1-8.